

## TEM microstructure of rapidly solidified Mg–6Zn–1Y–1Ce alloy

YANG Wen-peng<sup>1,2</sup>, GUO Xue-feng<sup>1</sup>, LU Zheng-xin<sup>2</sup>

1. School of Materials Science and Engineering, Henan Polytechnic University, Jiaozuo 454000, China;

2. School of Materials Science and Engineering, Xi'an University of Technology, Xi'an 710048, China

Received 22 March 2011; accepted 16 December 2011

**Abstract:** Rapidly solidified (RS) Mg–6Zn–1Y–1Ce ribbons were prepared by single roller melt-spinning technique. Transmission electron microscopy and energy dispersive X-ray spectroscopy were employed to characterize the microstructure of RS ribbons. The results show that there is high density of particles distributed within grains and at grain boundaries in the region near wheel side. The particle density is decreased in the middle region and free surface region. The alloy is predominantly composed of supersaturated  $\alpha$ -Mg solid solution, *T* phase and *W* phase; meanwhile, a few icosahedral quasicrystalline and Mg<sub>4</sub>Zn<sub>7</sub> particles are also observed. The *T* phase is confirmed having a body-centered orthorhombic structure that is transformed from the body-centered tetragonal structure Mg<sub>12</sub>Ce phase due to the partial substitution of Mg atoms by Zn.

**Key words:** Mg–6Zn–1Y–1Ce alloy; rapid solidification; *T* phase; icosahedral quasicrystalline; Mg<sub>4</sub>Zn<sub>7</sub> phase; *W* phase

### 1 Introduction

Mg alloys have great potential for high performance in aerospace and automotive applications owing to their low density, high specific strength and stiffness [1]. However, Mg alloys produced by traditional ingot metallurgy exhibit low strength, ductility and creep resistance due to coarse dendritic microstructure and brittle intermetallic networks at grain boundaries [2,3]. Thermomechanical treatments are effective to refine matrix microstructure by dynamic recrystallization, break the networks and make the strengthening particles redistribute within matrix and at grain boundaries [4–5]. In general, during deformation, however, the distribution of strengthening particles is not uniform and the particles are dispersed along deformation direction [6,7]. It was reported that the strengthening particles have strongly pinning effect on the moving of grain boundaries and therefore restrain the growth of fine recrystallized grains [8,9]. Hence, it is possible to achieve microstructure with finer grains if the strengthening particles are finer and the distribution of particles is more homogeneous. An

alternative way to refine the microstructure is using rapidly solidified powder metallurgy (RS/PM) technologies. It is found that strength has no remarkable improvement when applying RS/PM to conventional Mg alloys, such as ZK and AZ systems; however, RS/PM Mg alloys with the addition of rare earth elements (RE) show significant improvements on mechanical properties at room temperature and elevated temperatures due to the formation of high melting point intermetallic particles [10–15]. For Mg–Zn–RE system, Mg–Zn–Y–Ce alloys seem particularly promising because their microstructures are stable above 300 °C [11], and exhibit high strength and sufficient ductility depending on preparation process. RS/PM Mg–6Zn–1Y–0.6Ce–0.6Zr alloy prepared by extrusion has high tensile strength of 490–520 MPa and elongation of 6%–10% [13]. The alloy processed by reciprocating extrusion exhibits a high elongation of 27% and a high strength of 340 MPa. Interestingly, this alloy also shows two distinct yield points [10]. Besides the fine-grained microstructure, mechanical properties of materials mostly depend on the structural characteristics of their strengthening particles. Previous reports [11–13] comparatively studied the

**Foundation item:** Project (50271054) supported by the National Natural Science Foundation of China; Project (20070700003) supported by the Doctorate Programs Foundation of Ministry of Education of China; Project (102102210031) supported by the Science and Technologies Foundation of Henan Province, China; Project (2010A430008) supported by the Natural Science Foundation of Henan Educational Committee of China

**Corresponding author:** YANG Wen-peng; Tel: +86-391-3986906; E-mail: [wenpengy@gmail.com](mailto:wenpengy@gmail.com)

DOI: 10.1016/S1003-6326(11)61246-6

microstructures of RS Mg–Zn–Y and Mg–Zn–Y–Ce ribbons, and found that Ce plays an important role in the microstructural refinement and resultant improvement on mechanical properties of the consolidated materials due to the limited solubility of Ce in Mg. The XRD results suggested that the secondary phases in Mg–Zn–Y–Ce alloys are *W* and Mg<sub>17</sub>Ce<sub>2</sub> phases [12]. In this work, we report the structural characteristics of the secondary phases in RS Mg–6Zn–1Y–1Ce ribbon using transmission electron microscopy (TEM).

## 2 Experimental

A Mg–6Zn–1Y–1Ce ingot with a diameter of 52 mm and length of 120 mm was prepared by melting Mg (99.9%), Zn (99.9%), master alloys of Mg–47%Y and Mg–90%Ce in an electric resistance furnace at 720 °C under Ar+SF<sub>6</sub> atmosphere. The as-cast Mg–6Zn–1Y–1Ce alloy was remelted in a plain carbon steel crucible wrapped in a high frequency induction heating coil at 720 °C in a low Ar pressure of 440 Pa atmosphere, and then the melt was injected through a nozzle with a gap width about 1 mm onto the surface of a spinning copper wheel at a circumferential speed about 22 m/s. The thicknesses of the produced ribbons were about 100 μm. Cooling rate of the RS ribbons was estimated to be about  $1.65 \times 10^6$  °C/s according to the cooling rate function [16]. For analyzing microstructural evolution from wheel side (WS) to free cooling surface (FS), three TEM specimens were selectively ground to the WS and/or FS to 50 μm and twin-jet electron-polished to perforation in a solution (11.2 g Mg(ClO<sub>4</sub>)<sub>2</sub>+5.3 g LiCl+ 500 mL CH<sub>3</sub>OH+100 mL CH<sub>2</sub>H<sub>5</sub>OH) at –30 °C, finally ion-milled to remove the fine oxide film at an ion accelerating voltage of 4 keV. TEM observation was carried out using a JEM–3010 equipped with an Oxford Instruments energy-dispersive X-ray (EDX) spectrometer operating at 300 kV.

## 3 Results

Optical and scanning electron microscopy observations (not shown here) show that the microstructures of RSed ribbons between WS and FS regions are distinctly different. The thickness of WS region is 30–40 μm, which consists of coarse grains of 20–30 μm; the FS region has a thickness of 50–60 μm and consists of fine equiaxed grains with an average size of 4.5 μm. In addition, some ribbons contain a thin layer of no more than 10 μm in contacted to the wheel surface, which consists of fine grains less than 5 μm. The microstructural evolution from WS to FS of the RSed Mg–6Zn–1Y–1Ce alloy ribbon is much similar to that of

Mg–6Zn–1Y–0.6Ce–0.6Zr alloy [11]. The mechanism of microstructural evolution and the solidification process have been discussed elsewhere [12].

Figure 1(a) shows a bright-field (BF) TEM image taken from WS region. It is apparent that there is high density of fine particles distributed within grains and at grain boundaries. The dispersed particles are nearly spherical with an average diameter of 100 nm. A few

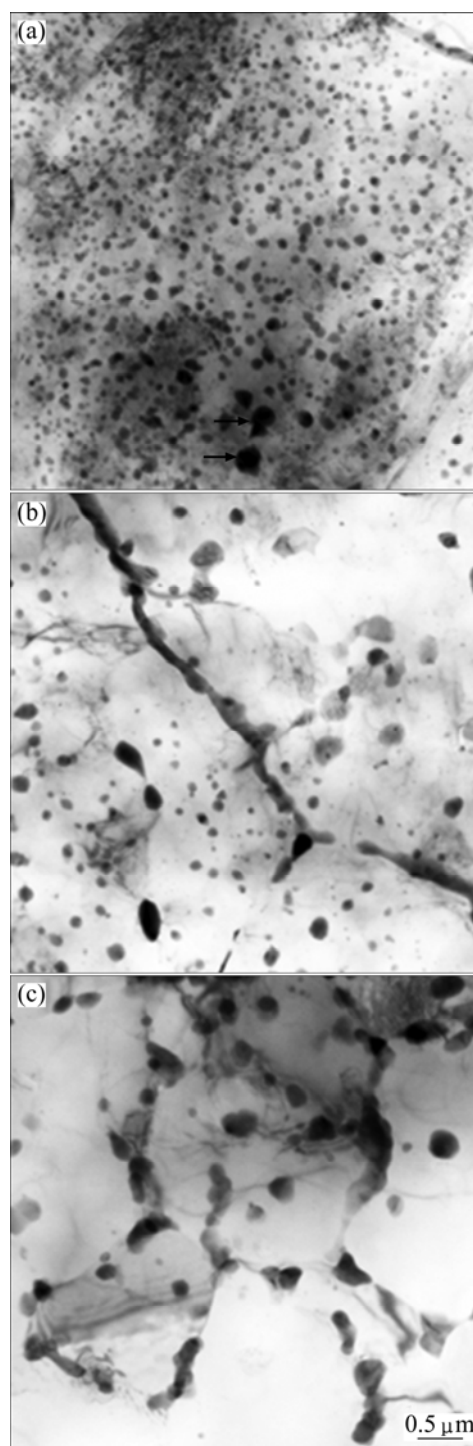


**Fig. 1** BF TEM images showing microstructures obtained from WS region (a), middle region (b) and FS region (c)

coarse particles with size of 100–200 nm also could be observed, as indicated by arrows in Fig. 1(a). At grain boundaries there are a few very thin strip-like intermetallic compounds. Figure 1(b) shows the TEM microstructure of middle region. In comparison with Fig. 1(a), the quantity of spherical particles is decreased. The particles in irregular shapes with size of 200–300 nm are observed in the matrix. The strip-like intermetallic compounds with thickness less than 250 nm are distributed at grain boundaries. In the FS region (Fig. 1(c)), the particles with size of 200–300 nm are

mostly distributed at grain boundaries, and a few particles are distributed within grains, and some grain interiors are free of particles. EDX spectra recorded from bright areas reveal that the  $\alpha$ -Mg solid solution is supersaturated with an average composition of Mg-(1.6%±0.3%) Zn (mole fraction). The particles in the RS ribbon were analyzed using EDX spectra and selected area electron diffraction (SAED) and four secondary phases are found.

An EDX spectrum (Fig. 2(b)) recorded from the particle indicated by an arrow in Fig. 2(a) reveals the

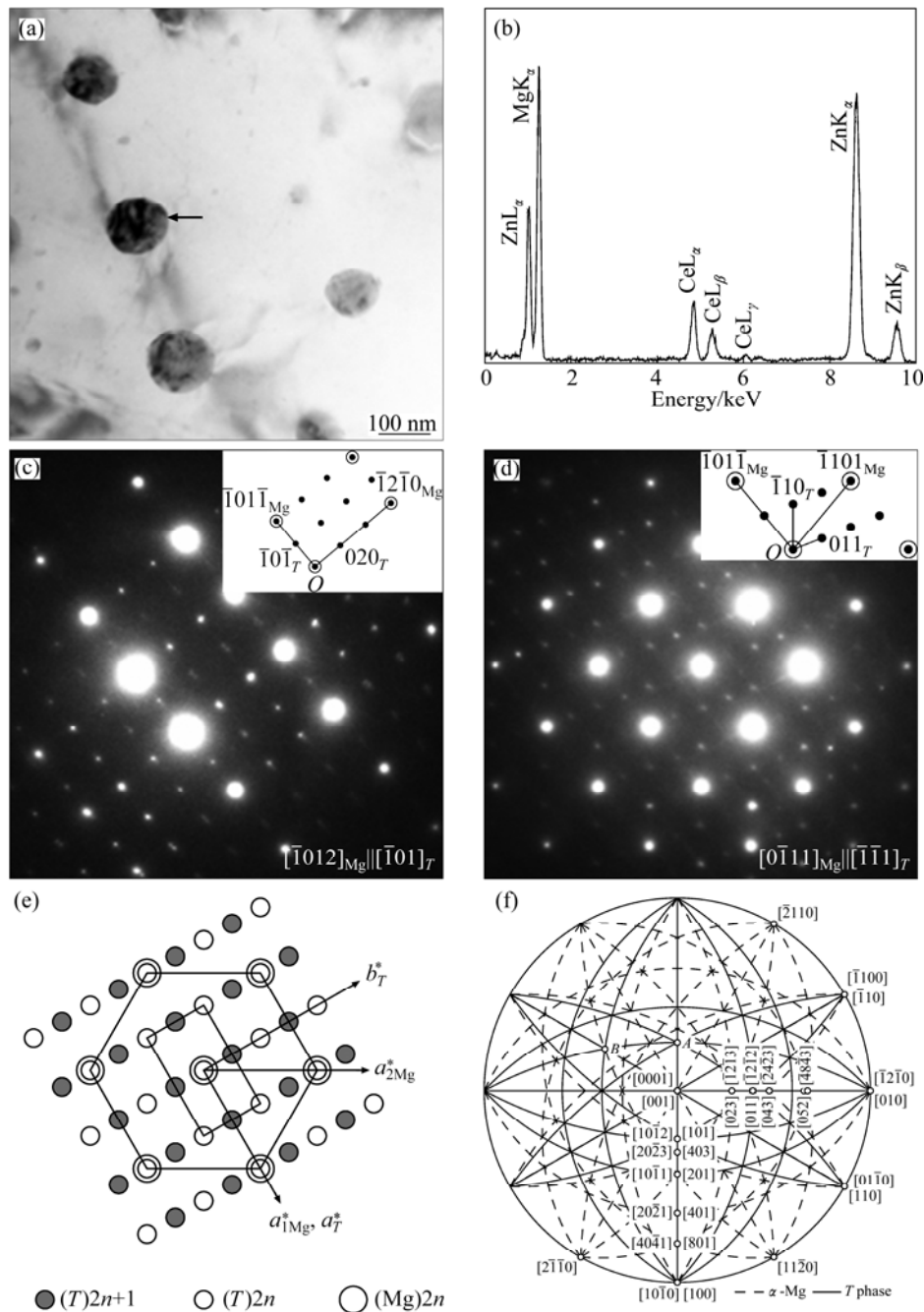


**Fig. 2** BF TEM image taken from WS region (a), EDX spectrum (b) recorded from particle indicated by arrow in Fig. 2(a), composite SAED patterns of particle and surrounding matrix taken from  $[\bar{1}012]_{\text{Mg}} \parallel [\bar{1}01]_{\text{T}}$  zone axis of Mg (c), composite SAED pattern taken from  $[0\bar{1}11]_{\text{Mg}} \parallel [\bar{1}\bar{1}1]_{\text{T}}$  zone axis after titling  $39.7^\circ$  along  $\{10\bar{1}\}_T$  vector from  $[\bar{1}012]_{\text{Mg}}$  zone axis (d), schematic diagram of composite reciprocal lattices of  $\alpha$ -Mg and T phase (e), and stereographic projects of  $\alpha$ -Mg and T phase for present orientation relationship (f)

prominent Mg  $K_{\alpha}$  and Zn  $K_{\alpha}$  peaks, significant intensity of Zn  $L_{\alpha}$  peak, and low intensities of Ce  $L_{\alpha}$ ,  $L_{\beta}$  and Zn  $K_{\beta}$  peaks. The composition is determined to be Mg–43.1% Zn–8.6% Ce (mole fraction). This is a new phase in this material and the phase is denoted as  $T$  phase in this study. We examined a number of  $T$  phase particles and found that the contents of Zn and Ce are in the ranges of 28.9%–45.3% and 7.6%–10.4%, respectively. The reason is discussed later. Figure 2(c) shows the composite SAED patterns recorded from the particle and surrounding matrix indicated by the arrow in Fig. 2(a). The strong diffraction spots are indexed consistently according to  $\alpha$ -Mg ( $a=3.09$  Å,  $c=5.00$  Å) with the electron beam (EB) parallel to  $[\bar{1}012]$  zone axis. The weak spots have perfect orientation relationships with matrix. However, the pattern of the  $T$  phase could not be indexed in the PDF database. Moreover, it is neither the  $\text{Th}_2\text{Ni}_{17}$  structure ( $a=10.10$  Å,  $c=9.97$  Å, space group  $P6_3/mmc$ ) as discussed in Ref. [17] nor the based-centered orthorhombic structure in Ref. [18]. The strong SAED spots shown in Fig. 2(d) are recorded from  $[0\bar{1}11]$  zone axis of  $\alpha$ -Mg that is arrived by tilting about  $39.7^\circ$  along the  $\{10\bar{1}1\}$  matrix vector from  $[\bar{1}012]$  zone axis. The SAED pattern of the particle also matches well with that of matrix.

According to the composite diffraction patterns in Figs. 2(c) and (d), a reciprocal space lattice of the  $T$  phase could be built based on the frame of the reciprocal lattice of Mg matrix. Figure 2(e) shows a schematic diagram of composite reciprocal lattices of matrix and  $T$  phase with their vectors  $c^*$  up perpendicular to paper. It is clear from Fig. 2(e) that the reflections of  $T$  phase satisfying the condition of  $h+k+l=2n+1$  are absent and that the reciprocal lattice shows a face-centered orthorhombic structure. Reversely, the corresponding crystal structure in real space is a body-centered orthorhombic structure. Hence, the diffraction patterns of  $T$  phase in Figs. 2(c) and (d) could be indexed according

to the analysis result of Fig. 2(e), as shown in the inserts in Figs. 2(c) and (d), respectively. In turn, the lattice parameters of  $T$  phase could be calculated ( $a=5.35$  Å,  $b=9.43$  Å,  $c=10.02$  Å, space group  $Immm$ ). With the lattice parameters of  $\alpha$ -Mg and  $T$  phase, we calculated the stereographic projects for the present orientation relationship, as shown in Fig. 2(f). Their orientation relationship is in the form of  $\langle 100 \rangle_T || \langle 10\bar{1}0 \rangle_{\alpha}$ ,  $\langle 010 \rangle_T || \langle \bar{1}2\bar{1}0 \rangle_{\alpha}$ ,  $\langle 001 \rangle_T || \langle 0001 \rangle_{\alpha}$ . The zone axes of matrix and  $T$  phase in Figs. 2(c) and (d) are pointed out in Fig. 2(f) by labels  $A$  and  $B$ , respectively.

The BF TEM image of particles is shown in Fig. 3(a) and Fig. 3(b) shows a typical EDX spectrum of the particle indicated by an arrow in Fig. 3(a). The EDX spectrum consistently shows strong Zn  $L_{\alpha}$  and  $K_{\alpha}$  peaks, moderate Mg  $K_{\alpha}$  and Y  $L_{\alpha}$  peaks. The composition is determined to be Mg–36.9%Zn–22.3%Y (mole fraction). The SAED pattern (the insert in Fig. 3(a)) could be indexed according to the face-centered cubic structure  $W$  phase ( $a=6.84$  Å, space group  $Fm\bar{3}m$ ) and the EB is parallel to  $[111]$  zone axis.

In Fig. 4(a), the particle indicated by an arrow also is composed of Mg, Zn and Y. Its EDX spectrum (Fig. 4(b)) shows prominent Zn  $L_{\alpha}$  and  $K_{\alpha}$  peaks; however, the intensity ratio of Y  $L_{\alpha}$  peak is significantly lower than that of  $W$  phase, as shown in Fig. 3(b). It is suggested that the particle contains low content of Y, and its composition is Mg–65.2%Zn–6.2%Y (mole fraction). The SAED pattern (the insert in Fig. 4(a)) recorded from the particle shows five-fold rotational symmetry. It could be identified that the particle is icosahedral quasicrystalline phase ( $I$  phase) with a calculated quasi-lattice constant  $a=5.02$  Å.

Figure 5(a) shows two polygonal particles whose EDX spectra have similar peaks. The EDX spectra consistently show prominent Zn  $L_{\alpha}$  and  $K_{\alpha}$  peaks, together with low intensity of Mg  $K_{\alpha}$  peak, and no detectable amount of Y and Ce are found. A representative

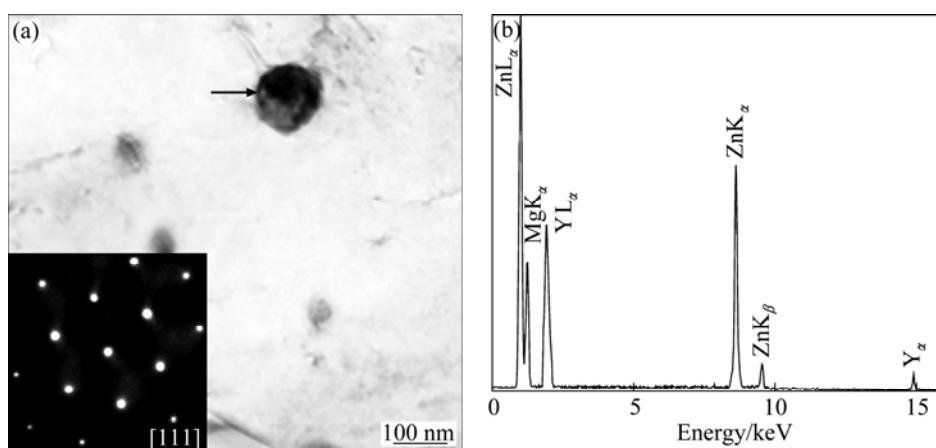


**Fig. 3** BF TEM image showing  $W$  phase particle indicated by arrow, and insert showing  $[111]$  zone SAED pattern (a), and EDX spectrum (b) recorded from particle indicated by arrow in Fig. 3(a)

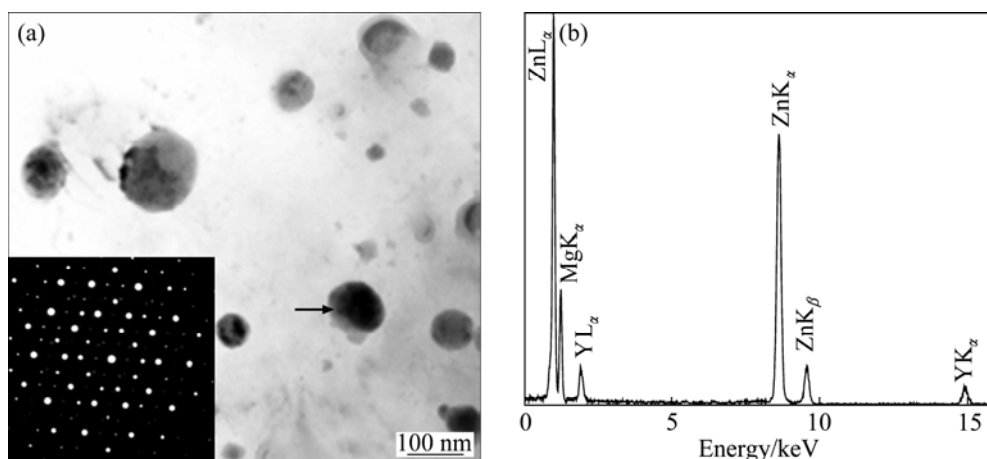


**Fig. 4** BF TEM image showing a *I* phase particle indicated by an arrow, and insert showing SAED pattern recorded from particle (a), and corresponding EDX spectrum (b) of particle in Fig. 4(a)

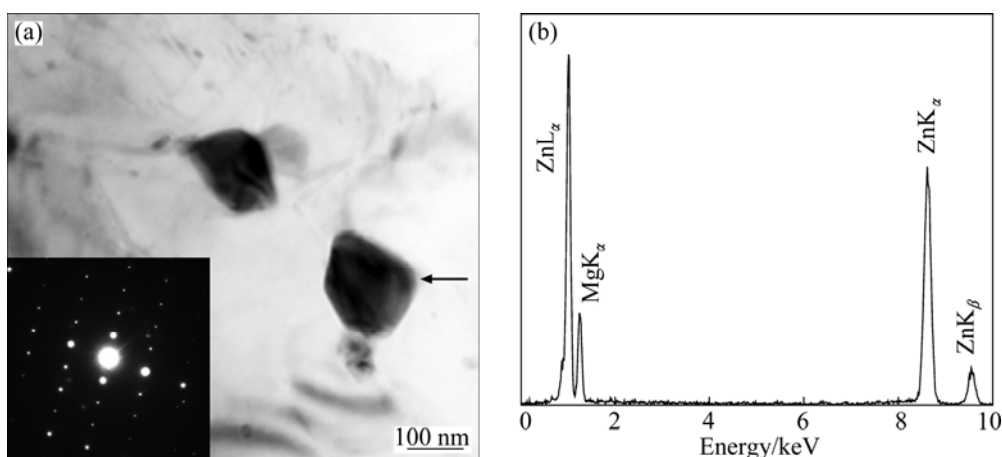


**Fig. 5** BF TEM image showing two polygonal  $Mg_4Zn_7$  particles, and insert showing SAED pattern recorded from right particle (a) and EDX spectrum (b) recorded from particle indicated by arrow in Fig. 5(a)

EDX spectrum recorded from the particle indicated by an arrow is shown in Fig. 5(a). The average composition is  $Mg-(70.6\pm 0.4)\% Zn$  (mole fraction). The SAED pattern (the insert in Fig. 5(a)) could be indexed according to the  $Mg_4Zn_7$  phase ( $a=25.96 \text{ \AA}$ ,  $b=14.28 \text{ \AA}$ ,  $c=5.24 \text{ \AA}$ ,  $\gamma=102.5^\circ$ , space group  $B2/m$ ) and the EB is close to  $[23\bar{2}]$  direction.

In RS  $Mg-6Zn-1Y-1Ce$  alloy it is found that the most particles are *T* phase and *W* phase, and a few *I* phase and  $Mg_4Zn_7$  phase particles are found. There have no given corresponding relationships between the shapes and phases. In addition, the thin strip-like intermetallic particles at grain boundary in the WS region are determined to be *T* phase by EDX spectra. However, the EDX microanalyses reveal that the compounds distributed at grain boundaries in Figs. 1(b) and (c) contain four elements. The average chemical composition is  $Mg-(32.8\pm 7.6)\%Zn-(10.7\pm 2.4)\%Y-(4.9\pm 2.2)\%Ce$  (mole fraction). At present, there have no

quaternary compounds have been reported. According to the previously results, it seems reasonable to conclude that the compounds are mixture of *T* phase and *W* phase.

## 4 Discussion

In the present RS alloy, only a few  $Mg_4Zn_7$  phase particles were observed, and  $Mg-Y$  and  $Mg-Ce$  binary phases were not found. Further, the rods, planes and blocky  $Mg-Zn$  precipitates, which were reported in  $Mg-Zn$  [19] and  $Mg-Zn-Y$  [20] alloys, were not found as well. Hence, the present alloy could be divided into two ternary subsystems:  $Mg-Zn-Ce$  and  $Mg-Zn-Y$ . By far, in  $Mg-Zn-Ce$  system, eight equilibrium phases were found:  $CeMg_7Zn_{12}$ ,  $Ce(Mg_{0.5-0.85}Zn_{0.15-0.5})_9$  (corresponding to *T* phase in the present study),  $CeMg_3Zn_5$  and  $Ce_2(MgZn)_3$  phases were reported by DRITS et al [21]; recently, KEVORKOV and PEKGULERGUZ [22] studied the  $Mg$ -rich corner at  $350 \text{ }^\circ C$  by using the

diffusion couple technique and found two new ternary phases,  $\text{Ce}_2\text{Mg}_{53}\text{Zn}_{45}$  and  $\text{Ce}_6\text{Mg}_{(8-15)}\text{Zn}_{(86-79)}$ ; in addition, PAVLYUK et al [23,24] reported a Heusler-type  $\text{CeMgZn}_2$  phase and a cubic  $\text{Mg}_{19}\text{Ce}_{20}\text{Zn}_{81}$  phase. Based on the EDX spectra results, the previous studies [18, 21, 22] consistently indicated that the  $T$  phase is a continuous substitutional solid solution of a binary Mg–Ce phase by exchanging Mg atoms with Zn, and the solid solubility limit of Zn is 48.49% at 350 °C [22]. However, there are two crystal structures proposed for  $T$  phase. DRITS et al [21] suggested that  $T$  phase is a solid solution of  $\text{Mg}_{17}\text{Ce}_2$  phase with the  $\text{Th}_{17}\text{Ni}_2$ -type structure, and HUANG et al [18] proposed a base-centered orthorhombic structure (the lattice parameters were not shown in their study), which is a solid solution of  $\text{Mg}_{12}\text{Ce}$  phase [22]. In comparison with previous studies, the present work identifies that  $T$  phase is a body-centered orthorhombic structure. Its calculated crystallographic data approximate to those of body-centered tetragonal structure  $\text{Mg}_{12}\text{Ce}$  phase ( $a=10.33$  Å,  $c=5.96$  Å, space group  $I4/mmm$ ). Since the radius of Zn atom (1.53 Å) is smaller than that of Mg (1.72 Å) atom, when Mg atoms are substituted by Zn, the lattice parameters should have a little decrease and the body-centered tetragonal structure could transform into body-centered orthorhombic structure. Therefore, it is confident to conclude that the  $T$  phase is the solid solution of  $\text{Mg}_{12}\text{Ce}$  phase. Further, it could be concluded that the more Zn atoms the  $T$  phase contains, the smaller lattice parameters the  $T$  phase has. It was reported that the compositions of  $T$  phase particles in the alloys prepared by diffusion couple techniques are uniform [18,22]. Therefore, the content deviations of Zn and Ce among  $T$  phase particles in the present study could be attributed to the nonequilibrium solidification process.

In Mg–Zn–Y system, depending on the mole ratio of Zn to Y there could have following ternary equilibrium phases:  $I$  phase ( $\text{Mg}_3\text{YZn}_6$ ),  $W$  phase ( $\text{Mg}_3\text{Y}_2\text{Zn}_3$ ), and long-period stacking ordered structures (including 6H, 14H and 18R etc) [25,26]. When the mole ratio of Zn to Y is between 5 and 7, the main secondary phase is  $I$  phase in both the as-cast [25] and the RS alloys [14]. In Mg–6Zn–1Y–1Ce alloy, the mole ratio of Zn to Y is about 6. However, the main Mg–Zn–Y ternary secondary phase is  $W$  phase. This is attributed to the addition of Ce, because during the nucleation and growth of  $T$  phase, a part of Zn atoms are consumed, which in turn decreases the mole ratio of Zn to Y. The calculated mole ratio of Zn to Y is in the range of 1–2 according to the compositions of  $\alpha$ -Mg and  $T$  phase, which favors the formation of  $W$  phase [25]. However, under the RS condition the distribution of solute is nonequilibrium, which leads to the possibility of formation of  $I$  phase and  $\text{Mg}_4\text{Zn}_7$  phase.

## 5 Conclusions

1) In the WS region, there is high density of particle distributed within grains and at grain boundaries. The particle density is decreased in middle region and FS region.

2) The secondary phase particles in RSed Mg–6Zn–1Y–1Ce alloy mainly are  $T$  phase and  $W$  phase; meanwhile a few icosahedral quasicrystalline and  $\text{Mg}_4\text{Zn}_7$  phase particles are observed.

3) The  $T$  phase has a body-centered orthorhombic structure ( $a=5.35$  Å,  $b=9.24$  Å,  $c=10.02$  Å, space group  $Immm$ ), a orientation relationship between  $T$  phase and matrix is  $\langle 100 \rangle_T \parallel \langle 10\bar{1}0 \rangle_\alpha$ ,  $\langle 010 \rangle_T \parallel \langle \bar{1}2\bar{1}0 \rangle_\alpha$ ,  $\langle 001 \rangle_T \parallel \langle 0001 \rangle_\alpha$ .

## References

- [1] EASTON M, SONG W Q, ABBOTT T. A comparison of the deformation of magnesium alloys with aluminum and steel in tension, bending and buckling [J]. Materials and Design, 2006, 27(10): 935–946.
- [2] XIAO W, JIA S, WANG L, WU Y, WANG L. The microstructures and mechanical properties of cast Mg–Zn–Al–RE alloys [J]. Journal of Alloys and Compounds, 2009, 480(2): L33–L36.
- [3] XIAO W, WANG J, YANG J, JIA S, WANG L. Microstructure and mechanical properties of Mg–12.3Zn–5.8Y–1.4Al alloy [J]. Materials Science and Engineering A, 2008, 485(1–2): 55–60.
- [4] HE S M, PENG L M, ZENG X Q, DING W J, ZHU Y P. Comparison of the microstructure and mechanical properties of a ZK60 alloy with and without 1.3% gadolinium addition [J]. Materials Science and Engineering A, 2006, 433(1–2): 175–181.
- [5] SOMEKAWA H, OSAWA Y, MUKAI T. Effect of solid-solution strengthening on fracture toughness in extruded Mg–Zn alloys [J]. Scripta Materialia, 2006, 55(7): 593–596.
- [6] LIU X B, CHEN R S, HAN E H. Effects of ageing treatment on microstructures and properties of Mg–Gd–Y–Zr alloys with and without Zn additions [J]. Journal of Alloys and Compounds, 2008, 465(1–2): 232–238.
- [7] YAMASAKI M, ANAN T, YOSHIMOTO S, KAWAMURA Y. Mechanical properties of warm-extruded Mg–Zn–Gd alloy with coherent 14H long periodic stacking ordered structure precipitate [J]. Scripta Materialia, 2005, 53(7): 799–803.
- [8] HOMMA T, KUNITO N, KAMADO S. Fabrication of extraordinary high-strength magnesium alloy by hot extrusion [J]. Scripta Materialia, 2009, 61(6): 644–647.
- [9] SASAKI T, YAMAMOTO K, HONMA T, KAMADO S, HONO K. A high-strength Mg–Sn–Zn–Al alloy extruded at low temperature [J]. Scripta Materialia, 2008, 59(10): 1111–1114.
- [10] GUO X, SHECHTMAN D. Reciprocating extrusion of rapidly solidified Mg–6Zn–1Y–0.6Ce–0.6Zr alloy [J]. Journal of Materials Processing Technology, 2007, 187–188: 640–644.
- [11] GUO X, REMENIK S, XU C, SHECHTMAN D. Development of Mg–6.0%Zn–1.0%Y–0.6%Ce–0.6%Zr magnesium alloy and its microstructural evolution during processing [J]. Materials Science and Engineering A, 2008, 473(1–2): 266–273.
- [12] GUO X, SHECHTMAN D. Extruded high-strength solid materials based on magnesium with zinc, yttrium, and cerium additives [J]. Glass Physics and Chemistry, 2005, 31(1): 44–52.

- [13] GUO X, KINSTLER J, GLAZMAN L, SHECHTMAN D. High strength Mg–Zn–Y–Ce–Zr alloy bars prepared by RS and extrusion technology [J]. *Materials Science Forum*, 2005, 488–489: 495–498.
- [14] MORA E, GARCÉS G, OÑORBE E, PÉREZ P, ADEVA P. High-strength Mg–Zn–Y alloys produced by powder metallurgy [J]. *Scripta Materialia*, 2009, 60(9): 776–779.
- [15] ŠUSTEK V, SPIGARELLI S, ČADEK J. Creep behavior at high stresses of a Mg–Zn–Ca–Ce–La alloy processed by rapid solidification [J]. *Scripta Materialia*, 1996, 35(3): 449–454.
- [16] WANG X J, CHEN X D, XIA T D, YU W Y, WANG X L. Influencing factors and estimation of the cooling rate within an amorphous ribbon [J]. *Intermetallics*, 2004, 12 (10–11): 1233–1237.
- [17] KOLITSCH U, BELLEN P, KAESCHKE S, MACCIÒ D, BOCHVAR N, LIBEROV Y, ROGL P. Cerium-magnesium-zinc [C]// EFFENBERG G, PETZOW G. Ternary Alloys—A Comprehensive Compendium of Evaluated Constitutional Data and Phase Diagrams. Weinheim, Stuttgart, Germany: VCH Verlagsgesellschaft MSI GmbH, 2000: 168–176.
- [18] HUANG M, LI H, DING H, REN Y, QIN G, HAO S. Partial phase relationships of Mg–Zn–Ce system at 350 °C [J]. *Transactions of Nonferrous Metals Society of China*, 2009, 19(3): 681–685.
- [19] GAO X, NIE J F. Characterization of strengthening precipitate phases in a Mg–Zn alloy [J]. *Scripta Materialia*, 2007, 56(8): 645–648.
- [20] SINGH A, TSAI A P. Structural characteristics of  $\beta_1'$  precipitates in Mg–Zn-based alloys [J]. *Scripta Materialia*, 2007, 57(10): 941–944.
- [21] DRITS M E, DROZDOVA E I, KOROL'KOVA I G, KINZHIBALO V, TYVANCHUK A T. Investigation of polythermal sections of the Mg–Zn–Ce system in the Mg-rich region [J]. *Russian Metallurgy (Metally)*, 1989, 2: 195–197.
- [22] KEVORKOV D, PEKGULERYUZ M. Experimental study of the Ce–Mg–Zn phase diagram at 350 °C via diffusion couple techniques [J]. *Journal of Alloys and Compounds*, 2009, 478(1–2): 427–436.
- [23] PAVLYUK V, SOLOKHA P, DMYTRIV G, MARCINIAK B, PAUL-BONCOUR V. The Heusler-type alloy MgZn<sub>2</sub>Ce [J]. *Acta Crystallographica: Section E*, 2007, 63(7): i161.
- [24] PAVLYUK V, SOLOKHA P, ZELINSKA O, PAUL-BONCOUR V, NOWIK ZAJAC A. Ce<sub>20</sub>Mg<sub>19</sub>Zn<sub>81</sub>: A new structure type with a giant cubic cell [J]. *Acta Crystallographica: Section C*, 2008, 64(7): i50–i52.
- [25] HUANG Z H, LIANG S M, CHEN R S, HAN E H. Solidification pathways and constituent phases of Mg–Zn–Y–Zr alloys [J]. *Journal of Alloys and Compounds*, 2009, 468 (1–2): 170–178.
- [26] LEE J Y, KIM D H, LIM H K, KIM D H. Effects of Zn/Y ratio on microstructure and mechanical properties of Mg–Zn–Y alloys [J]. *Materials Letters*, 2005, 59(29–30): 3801–3805.

## 快速凝固 Mg–6Zn–1Y–1Ce 合金的 TEM 组织

杨文朋<sup>1,2</sup>, 郭学锋<sup>1</sup>, 卢正欣<sup>2</sup>

1. 河南理工大学 材料科学与工程学院, 焦作 454000;

2. 西安理工大学 材料科学与工程学院, 西安 710048

**摘要:** 利用单辊甩带技术制备快速凝固 Mg–6Zn–1Y–1Ce 薄带, 并利用透射电子显微镜和能谱仪分析薄带组织。结果表明: 薄带近辊面区域晶粒内部和晶界处分布着高密度颗粒, 颗粒密度在中间区域和自由面区域有所降低; 快速凝固合金主要由过饱和的  $\alpha$ -Mg 固溶体、*T* 相和 *W* 相组成, 同时还存在少量的二十面体准晶相颗粒和 Mg<sub>4</sub>Zn<sub>7</sub> 相颗粒; 其中 *T* 相为体心正交晶体结构, 是由于体心正方结构的 Mg<sub>12</sub>Ce 相中部分 Mg 原子被 Zn 原子代替而形成的。

**关键词:** Mg–6Zn–1Y–1Ce 合金; 快速凝固; *T* 相; 准晶; Mg<sub>4</sub>Zn<sub>7</sub> 相; *W* 相

(Edited by LI Xiang-qun)